CRYSTAL Research&Technology
www.crt-journal.org

Morphologically and Compositionally Controlled Cs_2SbBr_6 by Bi and Ag Substitution

Alexander Frebel, Songhak Yoon, Samuel Meles Neguse, Dennis Michael Jöckel, Marc Widenmeyer, Stefan G. Ebbinghaus, Benjamin Balke-Grünewald, and Anke Weidenkaff*

Morphology-controlled Cs_2SbBr_6 crystals are synthesized by Bi- and Ag-substitution of the precursor solution. X-ray diffraction (XRD) together with Raman spectroscopy confirms the lattice tilting and symmetry changes with the dominant appearance of higher index facets by Bi substitution. Ag substitution does not induce crystal symmetry changes in the Cs_2BBr_6 (B = Sb or Bi) phase, but results in highly defective structures hindering the formation of a smooth surface during the crystal growth. Successful substitution of Bi and limited substitution of Ag into Cs_2SbBr_6 is also confirmed by energy dispersive X-ray spectroscopy (EDX). This research provides design principles and practical examples of how to control the morphology of Cs_2SbBr_6 crystals with structural defects and multiphase formation.

1. Introduction

Halide perovskite semiconductors are immensely investigated due to their compositional and functional flexibility and diversity. Especially, lead-based halide perovskites were found to be a promising material for photovoltaics (PV), although they are toxic and have limited stability.[1] Consequently, the investigation of perovskite derivatives such as double perovskites and vacancy-ordered perovskites including $Cs_2AgBiBr_6$, $Cs_3Bi_2Br_9$, $Cs_3Sb_2Br_9$, and Cs_2SbBr_6 widely opened the field of PV research.[2–4] Among them, Cs_2SbBr_6 shows unique structural properties due to the mixed oxidation states of Sb, Sb^{3+}, and Sb^{5+}.[5] The intrinsic properties of Cs_2SbBr_6, such as non-toxic composition compared to Pb-based perovskites and superior thermal stability, make it an attractive material for further investigation and optimization. Moreover, The coexistence of the two oxidation states also leads to a lattice distortion resulting in a tetragonal space group $I4_1/amd$ with the elongation of the axial bonds and the shortening of the equatorial bonds in octahedral $SbBr_6$ units.[6]

Recent research has focused on the substitution of various cations to change and enhance the structural, morphological, and electronic properties of Cs_2SbBr_6. To tailor the specific applications, for example, bismuth (Bi) and silver (Ag) are regarded as particularly interesting substitution elements due to their unique electronic configurations and ionic sizes, which can induce significant changes in the host lattice in Cs_2SbBr_6. Along with their use in photovoltaics, halide perovskites are widely employed as cathode materials or photocatalysts due to their unique but outstanding photochemical and photophysical properties.[7,8,9] Bismuth-based halide perovskites, for example, are known for their efficient toluene selective oxidation[9] and aromatic C—H bond activation.[8] Many factors in synthesis conditions such as the type of the solvent, chemical reaction rate, and additives have a consequential impact on the morphological change.[10,11] Notably, Swetha et al. summarized and reported the facet-dependent differently shaped nanostructures and their electrocatalytic behavior, emphasizing the need for facet-controlled nanocrystals for better catalysis.[12] Sun et al. discussed the effect of the crystal morphology in terms of photocatalysis and the potential effect due to different morphologies and the band bending resulting from facet junctions.[10]

The purpose of this work is to investigate how the substitution of Bi and Ag affects the morphological and compositional characteristics of Cs_2SbBr_6. By systematically controlling the substitution concentrations of Bi and Ag of the precursor solution and analyzing the obtained crystals through various characterization techniques, we aim to understand the interplay between substitution element type, concentration, and material properties. Specifically, we investigate the structural changes and surface morphology alterations induced by Bi and Ag substitution in Cs_2SbBr_6. Due to the mixed valence of Sb, different symmetries and crystal phases are expected to be possible by substituting on

A. Frebel, S. Yoon, S. M. Neguse, D. M. Jöckel, B. Balke-Grünewald, A. Weidenkaff
Fraunhofer Research Institution for Materials Recycling and Resource Strategies IWKS
Aschaffenburger Straße 121, 63457 Hanau, Germany
E-mail: Song.hak.yoon@iwks.fraunhofer.de
A. Frebel, M. Widenmeyer, A. Weidenkaff
Department of Materials and Earth Sciences
Technical University of Darmstadt
Peter-Grünberg-Straße 2, 64287 Darmstadt, Germany
S. G. Ebbinghaus
Institute of Chemistry
Martin Luther University Halle-Wittenberg
Kurt-Mothes-Strasse 2, 06120 Halle (Saale), Germany

DOI: 10.1002/crat.202400055

Table 1. Synthesized samples and their labeling based on the synthesis method and Bi and Ag precursor substitution ratio.

Sample label	Synthesis method	Bi substitution	Ag substitution
SM_0	Separate solutions, Microwave-assisted hydrothermal (SM)	0	0
M_0	Microwave-assisted hydrothermal [M]	0	0
M_B4	Microwave-assisted hydrothermal [M]	40%	0
M_B6	Microwave-assisted hydrothermal [M]	60%	0
M_B10	Microwave-assisted hydrothermal [M]	100%	0
M_A2	Microwave-assisted hydrothermal [M]	0	25%
M_A5	Microwave-assisted hydrothermal [M]		50%
M_A7	Microwave-assisted hydrothermal [M]		75%
M_B6A	Microwave-assisted hydrothermal [M]	60%	100%[a)]
M_B8A	Microwave-assisted hydrothermal [M]	80%	100%[a)]

[a)] In the co-substituted samples M_B6A, and M_B8A, Ag was added in the stoichiometric amount of the double perovskite composition.

the *B*-site in Cs_2SbBr_6 and $Cs_3B_2Br_9$ (B = Sb or Bi). With the crystal symmetry change, a morphology change is also anticipated with facilitated nucleation and crystal growth of different crystal systems. The findings from this research are expected to provide valuable insights into the design of high-performance halide perovskites with controlled morphological and compositional properties. This, in turn, could pave the way for the development of next-generation optoelectronic devices with enhanced efficiency, stability, and functionality.

2. Experimental Section

2.1. Synthesis

All samples were synthesized via microwave-assisted hydrothermal (M) synthesis using the microwave digestion system Turbowave 1500 (MLS Mikrowellen-Labor-Syteme GmbH). CsBr (99.9%, metal basis, Alfa Aesar), AgBr (99.5%, Alfa Aesar), $BiBr_3$ (99%, Alfa Aesar), $SbBr_3$ (99%, Alfa Aesar), and aqueous HBr solution (48%, Alfa Aesar) were used without further purification. 0.7 mmol of the precursors together with 9 ml HBr were placed in a Teflon-lined autoclave and heated to 200 °C within 10 min with a pressure of 4.7 MPa and kept at this temperature for a dwell time of 1 h. The solutions were then cooled down to 50 °C with a rate of 150 °C h^{-1}. The solutions were decanted. The obtained crystals were dried and stored in the air. All samples and their labels were listed together with the Bi- and Ag substitution amount in **Table 1**. The samples are denoted as M_B for Bi substitution and M_A for Ag substitution with the nominal substitution amount. In the Bi and Ag co-substituted samples AgBr is added in the stoichiometric amount of the double perovskite composition which were denoted as M_B6A, and M_B8A. In addition, Cs_2SbBr_6 is synthesized based on the report of Comb et al.[4] The precursor solutions of 0.9 mmol $SbBr_3$ in 9 ml HBr and 1.81 mmol CsBr in 5.5 ml HBr were produced separately by using the same temperature profile as described above. The prepared solutions were then mixed at room temperature (RT) under stirring and the black powder was ultimately collected and dried with filter paper.

2.2. Analysis

2.2.1. Scanning Electron Microscopy (SEM)

The particle sizes, their size distribution, and morphology were investigated by a field emission scanning electron microscope (FE-SEM, Carl Zeiss) equipped with an X-Max large area EDS detector (Oxford Instruments) operating at an accelerating voltage of 8 kV. For the determination of the crystal composition, energy dispersive X-ray spectroscopy (EDX) was carried out. In order to obtain the emission of characteristic X-rays from a specimen, a high-energy beam of electrons with an excitation energy of 25 keV was applied.

2.2.2. X-ray Diffraction (XRD)

The powder X-ray diffraction (XRD) patterns were obtained using a *Malvern PANalytical Empyrean* diffractometer (Co-$K\alpha_{1,2}$ radiation) to identify the various phases present in the synthesized samples. The diffraction patterns were recorded in a 2θ range of 10° and 100° with an angular step interval of 0.013°. XRD patterns were analyzed with the Le Bail method incorporated in the Rietveld refinement program *FullProf* to determine the lattice parameters. The Thompson-Cox-Hastings pseudo-Voigt function was chosen as the profile function.

2.2.3. Raman Spectroscopy

Raman spectra were obtained at room temperature using a Bruker SENTERRA Raman microscope. The samples were excited with a He-Ne laser with 20 mW power at an excitation wavelength of 632.8 nm, which was focused on the sample surfaces through an optical microscope unit. An objective lens with a magnification of 20 and an aperture of 25 µm was chosen. The spectral resolution was 2 cm^{-1} over a measured range of 50–300 cm^{-1}.

3. Results

The morphology changes of Cs_2SbBr_6 by Bi and Ag precursor substitution are depicted in **Figure 1**. Starting at the top left corner of Figure 1 with the unsubstituted sample M_0, the successful formation of the 2D-like perovskite microplate structures with a hexagonal shape, smooth surface, and high crystalline quality were found for $Cs_3Sb_2Br_9$ as shown in Figure 1a, beside the Cs_2SbBr_6 crystals Figure 1b.[13] The notable difference was observed for Cs_2SbBr_6 with an octahedral shape due to the formation of the vacancy-ordered perovskite. Cs_2SbBr_6 single crystals revealed two different shapes as shown in Figure 1b of the more Cs_2SbBr_6 pure sample SM_0, indicating together with (a) the two possible crystal structures of the Sb halide perovskite. Due to different bond lengths caused by the different ionic radii of the two possible oxidation states of Sb, different facets are developed compared to the other octahedra-shaped crystals of Bi- and Ag-based double perovskites. Double perovskites, e.g., $Cs_2AgBiBr_6$ (Figure 1 i) have a cubic structure, while Cs_2SbBr_6 is known to have a tetragonal crystal system.[4] $Cs_3Sb_2Br_9$ is reported to

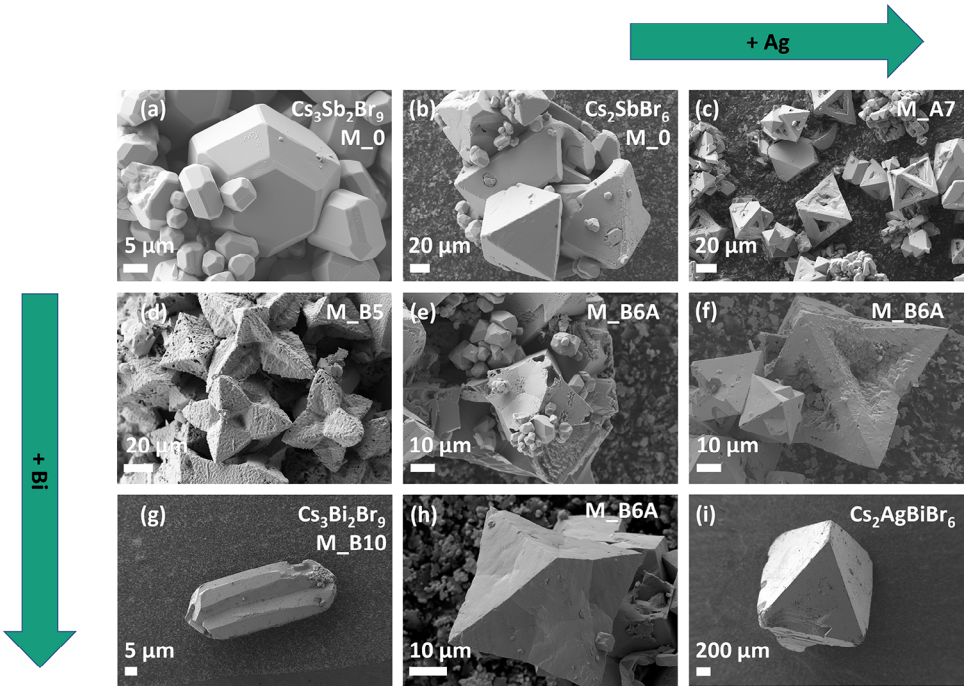

Figure 1. SEM images of synthesized crystals including a) $Cs_3Sb_2Br_9$, b) Cs_2SbBr_6, g) $Cs_3Bi_2Br_9$, and i) $Cs_2AgBiBr_6$. In between the samples with Bi-substituted d)–f), h)) and Ag substituted c), e), f), h)) Cs_2SbBr_6 and $Cs_3Sb_2Br_9$ are presented.

have a hexagonal crystal structure with a hexagonal microplate shape. Interestingly, partial substitution of Bi with Sb shown in Figure 1d,e,f,h (Samples M_B5 and M_B6A) resulted in concave octahedra or star shape polyhedra, that tend to form dendrites without Ag in Figure 1d. Furthermore, the surface is not smooth, but porous with a certain directional arrangement of a needle structure with a specific connecting angle (Figure 1d). As shown in Figure 1g with the Bi pure sample M_B10, $Cs_3Bi_2Br_9$ is then again grown in hexagonal shape but more expanded on one axis compared to unsubstituted $Cs_3Sb_2Br_9$. Ag substitution for Sb as shown in Figure 1c (sample M_A7) reoriented the crystal shape to be octahedral. Instead of completely formed octahedra, the facet development is found to be incomplete with remaining pores. The crystals are grown in round stairs. Lastly, substitution by both Ag and Bi for Sb shown in Figure 1e,f,h led to concave and incompletely formed single crystals and therefore a combination of both phenomena induced by Bi and Ag precursor substitution.

In order to clarify the reason for the formation of such different morphologies depending on the precursor ratio, XRD measurements were conducted to investigate the phase purity, crystal structures with varied symmetry, and growth orientation changes in Cs_2SbBr_6 and $Cs_3Sb_2Br_9$ by Bi and Ag substitution. The XRD patterns of Bi substitution are shown in **Figure 2**a. For unsubstituted Cs_2SbBr_6 (SM_0) all observed reflections were indexed to a tetragonal structure with space group $I4_1/amd$.[14,15] For $Cs_3Sb_2Br_9$ (M_0), all of the reflections correspond to the hexagonal structure with the space group $P\bar{3}m1$.[16] The partial Bi substituted sample shown is M_B4, which resulted in interesting morphological changes with concave octahedra and star-shaped polyhedra. The samples SM_0 and M_0 clearly show the reflections of the Cs_2SbBr_6, and $Cs_3Sb_2Br_9$ phases. Hereby in sample M_0, the reflections of the $Cs_3Sb_2Br_9$ phase were more defined, whereas it also showed traces of the Cs_2SbBr_6 phase. M_B10 clearly showed the reflections of the hexagonal $Cs_3Bi_2Br_9$ phase. The partially Bi substituted sample showed a phase mixture, the reflections of the Cs_2BBr_6 and $Cs_3B_2Br_9$ (B = Sb or Bi). Furthermore, the reflections were broader compared to the unsubstituted samples and shifted to a lower diffraction angle. In the case of Ag substitution (shown in Figure 2b), the Bragg angles of the Cs_2SbBr_6 phase stayed constant, and small reflections of $Cs_3Sb_2Br_9$ can be distinguished. The match of those reflections was not satisfactory with $Cs_2AgSbBr_6$, although the formation of double perovskite phase $Cs_2AgSbBr_6$ seems likely to be possible based on the precursor stoichiometry. The diffraction peaks get significantly broadened showing that the crystallinity decreases with Ag substitution. Figure 2c revealed a similar trend for the samples substituted with both Bi and Ag. The reflections were broadened and shifted toward a lower diffraction angle. It should be noted that the intensities of higher facet reflections were increased in the substituted samples. Extended XRD patterns are shown in Figure S1 (Supporting Information).

The lattice parameters derived from Le Bail fitting results are listed in Table S2 in Supporting information S2. Hereby the tetragonal Cs_2BBr_6 with the space group $I4_1/amd$ (B = Sb or Bi) were chosen for the model systems. The resulting estimated lattice parameter a and c/a ratio for a tetragonal phase of Cs_2BBr_6 are illustrated in Figure S2 (Supporting Information) Bi and Ag substitution. Bi led not only to an increase of the lattice parameter a but also to a decrease of the c/a ratio as shown in Figure S2a.(Supporting Information) In the case of Ag substitution, no change can be identified (Figure S2b, Supporting Information).

Raman spectroscopy was conducted in order to investigate the change in the short-range ordering of the crystal structure and the symmetry change as well as crystal perfection. The Raman

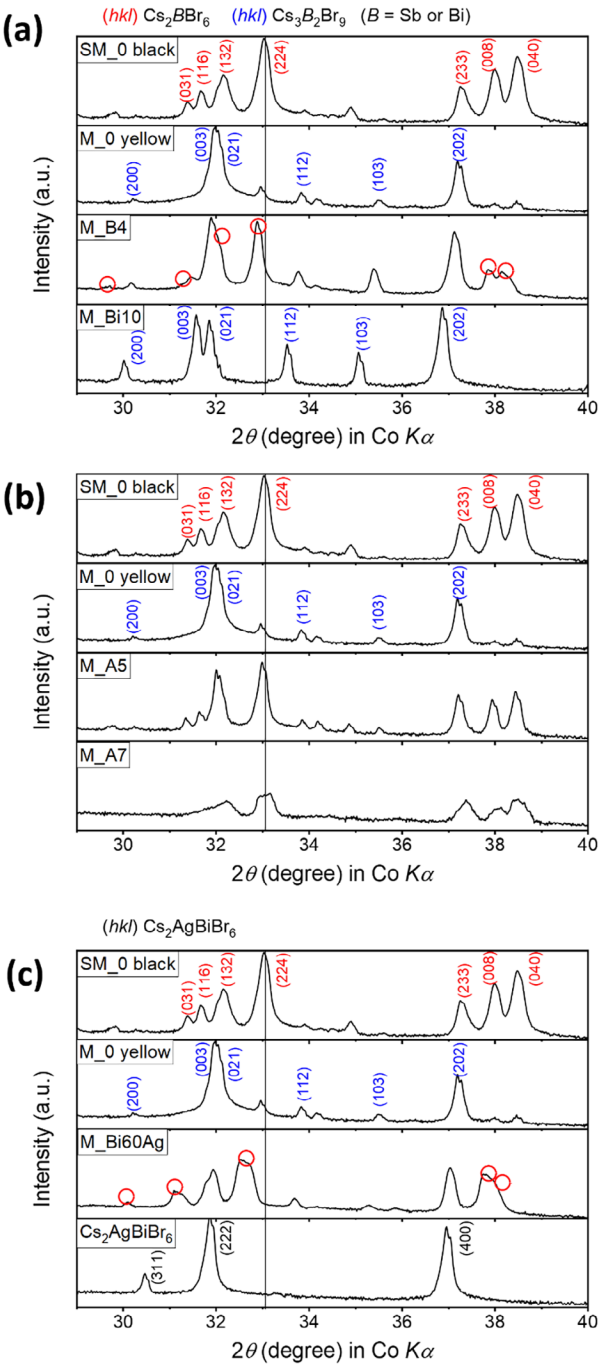

Figure 2. XRD patterns of the 3 substitution paths of Cs_2SbBr_6: a) Bi substitution, b) Ag substitution, and c) both Bi and Ag substitution. All patterns are plotted with a logarithmic ordinate. The drawn line indicates the reflection angle of the (224) plane of Cs_2SbBr_6 of the Sb pure sample. The red circles indicate the reflections that can be assigned to the Cs_2BBr_6 phase (B = Sb or Bi) in the substituted samples.

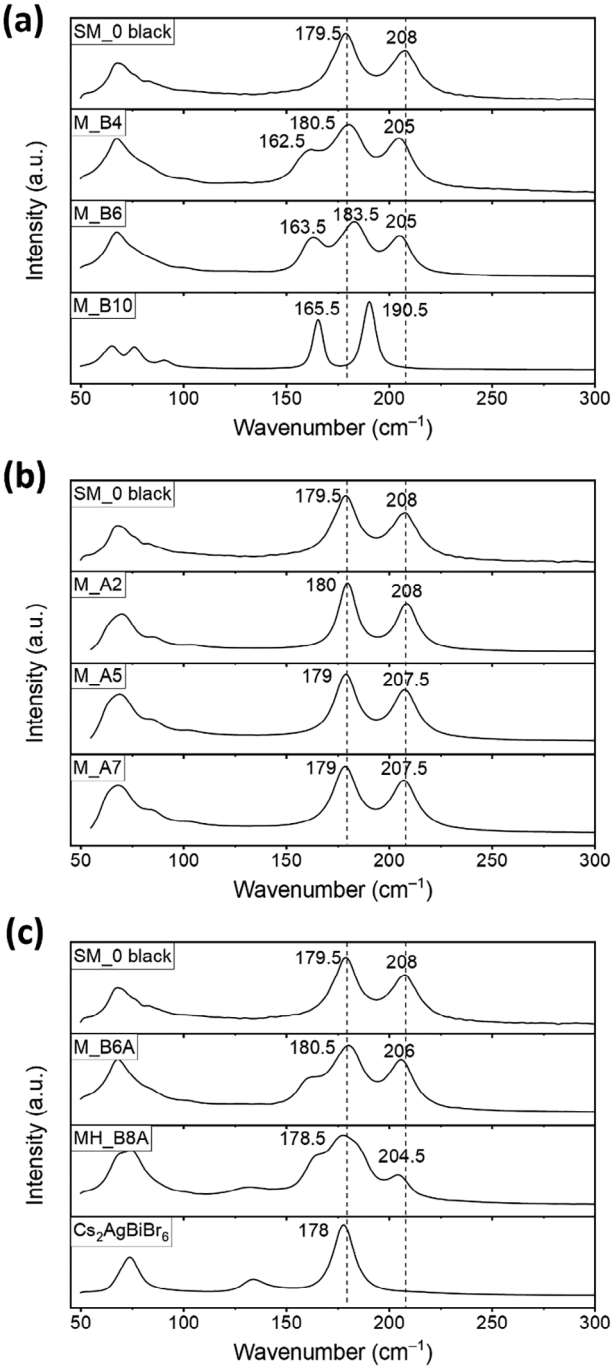

Figure 3. Raman spectra of the 3 substitution paths of Cs_2SbBr_6: a) Bi substitution, b) Ag substitution, and c) Bi+Ag substitution. The black dashed lines indicate the positions of the E_g, and A_{1g} band of the Cs_2SbBr_6 phase.

spectra of the 3 different substitution paths of Cs_2SbBr_6 are shown in **Figure 3**. The Raman spectrum of Cs_2SbBr_6 contained three main vibration modes of 70, 179.5, and 208 cm^{-1} assigned to be F_{2g}, E_g, and A_{1g}. These are similar to the bands which can be observed for $Cs_3Sb_2Br_9$.[16–18] The Bi substitution led to the appearance of an additional band at 162.5 cm^{-1} as shown in Figure 3a. This confirms the appearance of the E_g band of the Bi octahedra in the short-range ordering. The band at 179.5 cm^{-1} convolutes with the A_{1g} band of the Bi-Br bonding, which becomes broadened and shifts to a higher wavenumber. The band position of A_{1g} of the Sb-Br bonds was shifted to the lower wavenumber after Bi substitution. Interestingly, Ag substitution

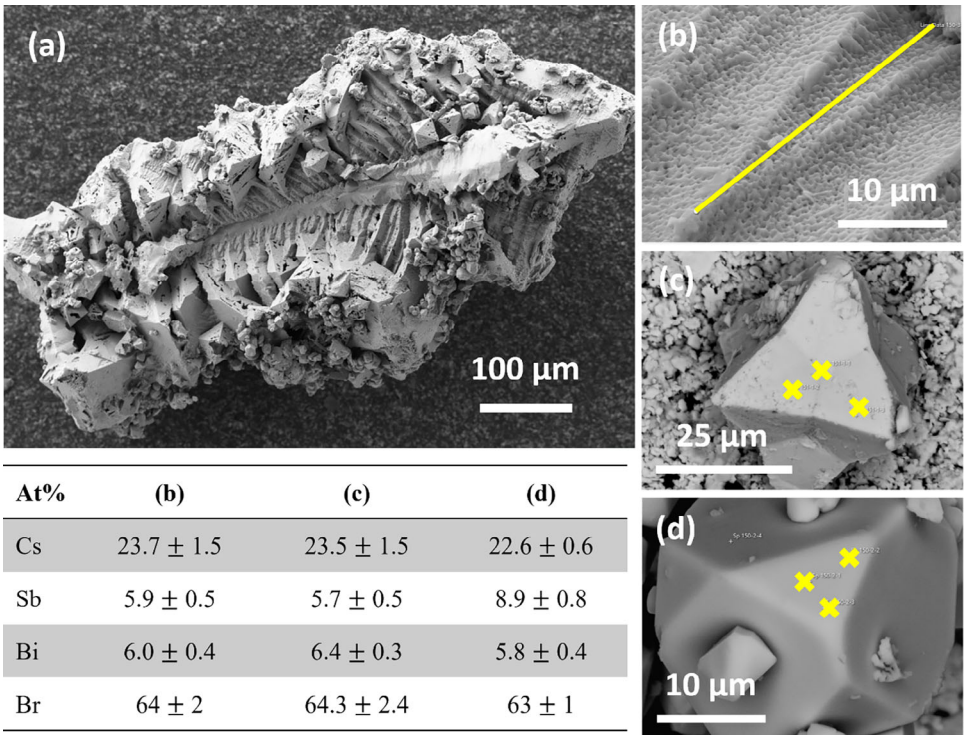

At%	(b)	(c)	(d)
Cs	23.7 ± 1.5	23.5 ± 1.5	22.6 ± 0.6
Sb	5.9 ± 0.5	5.7 ± 0.5	8.9 ± 0.8
Bi	6.0 ± 0.4	6.4 ± 0.3	5.8 ± 0.4
Br	64 ± 2	64.3 ± 2.4	63 ± 1

Figure 4. a) SEM image of a representative agglomerate of an incompletely formed single crystal of sample M_B4A, b) EDX line scan in M_B6, c) EDX point measurements in M_B6A2 and d) M_B6 of selected single crystals. The table shows the average atomic composition ratio for each crystal.

for Sb did not change the band position of Cs_2SbBr_6 and only peak broadening of the bands was observed, indicating a more defective structure (Figure 3b).[2,19] Hence, a highly defective structure due to Ag substitution could be confirmed (Figure 3b). As shown in XRD (Figure 2b) the Ag substitution had no effect on the lattice parameter and showed therefore no change in the vibration mode in the Raman spectroscopy. The in XRD partially matched $Cs_2AgSbBr_6$ structure could not be confirmed by Raman spectroscopy, as the E_g Raman band of the double perovskite structure does not appear at lower wavenumber. Substitution by both Bi and Ag-induced shoulders at the E_g band of the Sb-Br bonds (Figure 3c). These are due to the formation of Bi octahedra. The A_{1g} band of the Sb-Br bonds shifted toward a lower wavenumber. Mean band position and broadening were analyzed and are exhibited in the Supporting information S3. In addition, a comparison of A_{1g} bands of both possible structures, Cs_2SbBr_6 and $Cs_3Sb_2Br_9$, is shown in the Supporting information S4. In the $Cs_3Sb_2Br_9$ structure, the A_{1g} band was measured at the wavenumber of 210 cm^{-1}. Also, in this case, the broadening was smaller than in the case of pure Cs_2SbBr_6. Two oxidation states of Sb coexist in Cs_2SbBr_6,[4] whereas only Sb^{3+} exists in $Cs_3Sb_2Br_9$.[16,18] Therefore, one of the possible explanations for the increased broadening in Cs_2SbBr_6 can be the coexistence of two oxidation states of Sb. As reported by Combs et al.[4] the average bond lengths of Sb-Br are 2.784 Å for Sb^{3+} and 2.577 Å for Sb^{5+} at room temperature. This would suggest that the band caused due to the Sb^{5+} bonding vibrations should be at a higher wavenumber with a shorten bond length.[20] The two different bond lengths of Sb and a shift due to the valence electron transfer between the two oxidation states can have a major impact on the shift of band wavenumber.[17,21] Consequently, the A_{1g} band of the Sb-Br bonds in the Bi substituted sample was shifted further to lower wavenumber, because of the larger ionic radius of Bi^{3+} compared to Sb^{3+}.[17,20] The change in short-range bonding shown via Raman spectroscopy resulting from Bi substitution is in good agreement with the determined change in long-range ordering in the XRD measurement. By increasing Bi^{3+} substitution for Sb^{3+}, the concentration of Sb^{3+} decreased leading to Sb^{5+} being the dominant Sb oxidation state. This results in a more cubic symmetry without lattice contraction.

The compositions of the single crystals were determined by energy-dispersive X-ray spectroscopy (EDX) and an agglomerate with various morphology motifs is exemplarily exhibited in **Figure** 4a. Representative EDX line scan and point measurements of the occurring motif crystal types in the agglomerate are shown in Figure 4b–d. Figure 4b shows the crystal morphology which usually occurs in the center of the agglomerates. Besides the dendrite-like growth, it was notable that the surface texture was defined with structures attached to each other. The same texture can be observed for the concave star-shaped crystals (Figure 1d). Interestingly, the average composition determined by a line scan shows a clear Cs_2BBr_6 stoichiometry with a shared *B*-site of 50% of Sb and 50% of Bi. Independent of the precursor stoichiometry these resulting porous structures show a 1:1 ratio of Bi and Sb. The concave polyhedra shown in Figure 4c seem to be attached to the crystal shown in Figure 4b. Crystallites with smooth surfaces were found to grow on top of different crystals. The structure found in Figure 4d showed a hexagonal shape which can be explained by the given crystal symmetry of the hexagonal $Cs_3B_2Br_9$ phase. The crystals with a smooth surface

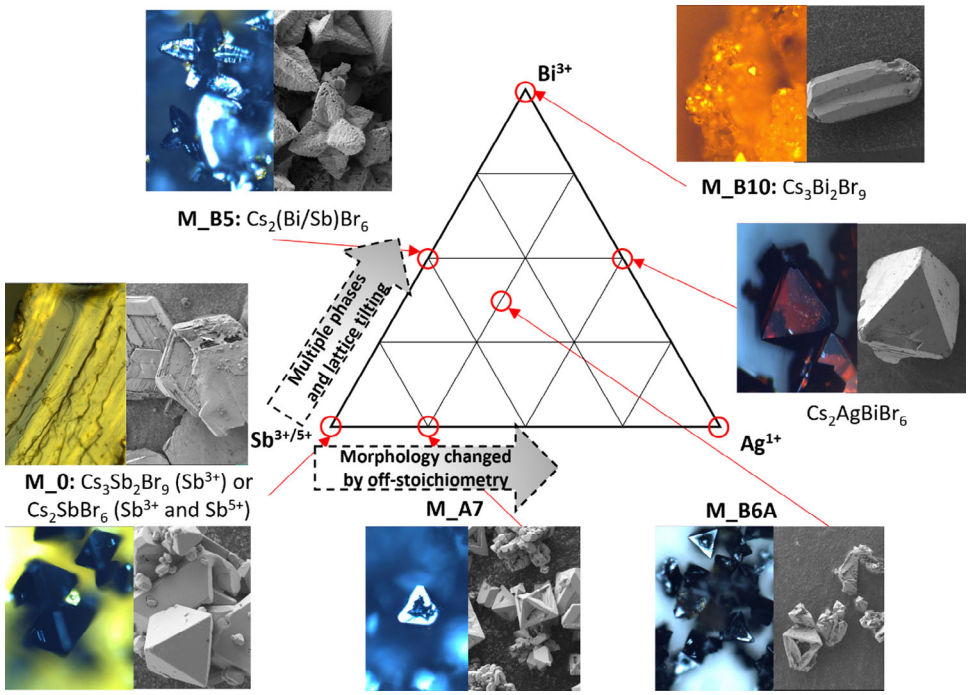

Figure 5. Schema of the morphology dependence on the stoichiometry. The grid shows the atomic ratio obtained by EDX on the *B*-site. The grey arrows indicate the occurring phenomena.

have a surplus of Sb. Further EDX point analyses are summarized in the Supporting information S5, revealing that there is a clear correlation between morphology and composition of the resulting crystals. Homogeneous and nonporous octahedral crystals were all found to exhibit a Cs_2SbBr_6 stoichiometry. Concave octahedral and dendrites with triangular needle structures have a *B* site sharing of both Bi and Sb with an approximate ratio of 1:1. A surplus of Sb leads to smaller tilting angles and homogeneous surfaces. In general, the shown crystal stoichiometries are dependent on the ratio of the different crystal types changes with the Bi/Sb content of the precursor. The increasing Ag substitution leads to the production of non-stoichiometric crystals, which are imperfectly and incompletely grown. In other words, due to the defects by non-stoichiometry in the Ag substituted samples, island-like grown crystals formed. The more defective structures are also confirmed for Ag substitution by SEM, XRD, and Raman spectroscopy. Thus, it is concluded that the developed morphologies of Cs_2SbBr_6 by Bi and Ag substitution are a result of sequential phase formation due to different motifs and defects during the synthesis.

4. Discussion

The morphology of Cs_2SbBr_6 is controlled by adding Bi and Ag into the precursor solution. Crystal growth mechanisms based on the obtained changes in microstructures, crystal structures, and stoichiometries are mapped in **Figure 5**. The Bi-substituted samples are found by XRD to be a mixture of two crystal phases, namely Cs_2BBr_6 and $Cs_3B_2Br_9$ (B = Sb or Bi). Both phases are nucleated and grown to agglomerates during the synthesis. Thus, the Bi-substituted crystals formed an agglomeration and oriented attachment of mainly two phases. Presumably, yellow $Cs_3B_2Br_9$ precipitates first, forming a porous dendrite grid of a mixed phase, and afterward Cs_2BBr_6 is formed during the solution cooled down to room temperature. This was also reported by Lin et al. who suggested that the Cs_2BBr_6 phase is only formed at room temperature.[15] EDX measurements in our study also confirmed that the agglomerates consisted of the Cs_2BBr_6 phase in the center and $Cs_3B_2Br_9$ phases attached at the surface as shown in Supporting information S5. It is concluded that the first formed $Cs_3B_2Br_9$ acts as a nucleation center and transforms due to the cooling of the solution to Cs_2BBr_6. This would explain the needle-like texture of the crystals at the surface as the $Cs_3B_2Br_9$ phase tends to grow in an anisotropic shape which is governed by the crystal structure and symmetry.

Based on the observations by XRD, it can also be deduced that within the Cs_2BBr_6 phase, a lattice distortion occurs due to Bi substitution, which was indicated by the Le Bail fit of the shifted reflections. The broadening of the reflections indicated the possible existence of an intermediate phase with lower crystallinity. The morphology change within the Cs_2BBr_6 phase would then be a result of lattice tilting between the tetragonal Cs_2BBr_6 and the hexagonal $Cs_3B_2Br_9$, which have different facets in the crystal growth.[16] This would be in excellent agreement with previous literature on single crystals with high-index facets.[10,12,22]

The Ag substitution stabilized the Cs_2BBr_6 phase formation and prevented the formation of secondary phases. No changes in the lattice and crystal symmetry, as confirmed by XRD and Raman spectroscopy, are supported by no noticeable tilting between the crystal branches. Nevertheless, the defective structure

shown by the reflection broadening is linked to the incomplete crystal formation.[23] These broadening phenomena in XRD can also reflect a crucial part of the formation process for both Bi and Ag-substituted samples. Therefore, Ag substitution leads to more defective and less crystalline samples compared to Bi substitution. Furthermore, the EDX measurements revealed that Ag can hardly substitute Sb and led only to off-stoichiometry. Our results showed no sign of the formation of a $Cs_2AgSbBr_6$ double perovskite in the applied synthesis set-up despite providing both Ag and Sb in M_A7. Ag substituted samples showed concave octahedra without filling the octahedral surfaces. These crystals also do not show star shape. It can be concluded that the defective structure of Ag-substituted samples hinders the diffusion process of the filling of the crystal surface.

5. Summary

The morphology of Cs_2SbBr_6 was controlled via Bi and Ag precursor substitution in the solution. Bi^{3+} is found to substitute Sb^{3+} in mixed valence Cs_2SbBr_6 lattice leading to the preferred growth of star shape polyhedra and concave octahedra with two-phase mixtures of Cs_2BBr_6 and $Cs_3B_2Br_9$ (B = Sb or Bi). In contrast, Ag substitution is limited in Cs_2SbBr_6 leading to incompletely shaped octahedra. The smooth surface formation is suppressed and the formation of $Cs_3B_2Br_9$ (B = Sb or Bi) phase is prevented for the samples substituted with both Bi and Ag together. The exemplarily shown substitution strategy in this study can be also applied to the synthesis of other mixed valence Sb-based halide perovskite-type materials.

Supporting Information

Supporting Information is available from the Wiley Online Library or from the author.

Acknowledgements

The authors thank Jürgen Rossa for providing the SEM and EDX measurements and for the scientific discussion and helpful comments. This work was financially supported by Fraunhofer Lighthouse Project MaNiTU – Materials for sustainable tandem solar cells with extremely high conversion efficiency.

Open access funding enabled and organized by Projekt DEAL.

Conflict of Interest

The authors declare no conflict of interest.

Data Availability Statement

The data that support the findings of this study are available from the corresponding author upon reasonable request.

Keywords

Cs_2SbBr_6, $Cs_3Sb_2Br_9$, Morphology change, Oriented attachment, Raman spectroscopy, X-ray diffraction

Received: February 20, 2024
Revised: July 28, 2024
Published online: September 18, 2024

[1] a) M. A. Green, A. Ho-Baillie, H. J. Snaith, *Nature Photon* **2014**, *8*, 506; b) A. Babayigit, A. Ethirajan, M. Muller, B. Conings, *Nat. Mater.* **2016**, *15*, 247.
[2] A. Frebel, S. Yoon, S. Meles Neguse, D. M. Jöckel, M. Widenmeyer, S. Lange, V. Naumann, A. Rosspeintner, S. G. Ebbinghaus, B. Balke, A. Weidenkaff, *Advanced Photonics Research* **2022**, *3*, 2200061.
[3] S. Yoon, B. Fett, A. Frebel, S. Kroisl, B. Herbig, M. Widenmeyer, B. Balke, G. Sextl, K. Mandel, A. Weidenkaff, *Energy Technol.* **2022**, *10*, 2200197.
[4] V. E. Combs, I. W. H. Oswald, J. R. Neilson, *Cryst. Growth Des.* **2019**, *19*, 4090.
[5] M. F. Summers, P. J. Toscano, N. Bresciani-Pahor, G. Nardin, L. Randaccio, L. G. Marzill, *J. Am. Chem. Soc.* **1983**, *105*, 6259.
[6] K. Prassides, P. Day, A. K. Chandiran, *Inorg. Chem.* **1985**, *24*, 545.
[7] a) Y. Han, Y. Lei, J. Ni, Y. Zhang, Z. Geng, P. Ming, C. Zhang, X. Tian, J. L. Shi, Y.-G. Guo, Q. Xiao, *Small* **2022**, *18*, e2107048; b) K. Chen, X. Deng, G. Dodekatos, H. Tüysüz, *J. Am. Chem. Soc.* **2017**, *139*, 12267.
[8] Y. Dai, C. Poidevin, C. Ochoa-Hernández, A. A. Auer, H. Tüysüz, *Angew. Chem.* **2020**, *132*, 5837.
[9] Z. J. Bai, X. P. Tan, L. Chen, B. Hu, Y. X. Tan, Y. Mao, S. Shen, J. K. Guo, C. T. Au, Z. W. Liang, S. F. Yin, *Chem. Eng. Sci.* **2022**, *247*, 116983.
[10] S. Sun, L. He, M. Yang, J. Cui, S. Liang, *Adv. Funct. Mater.* **2022**, *32*, 2106982.
[11] a) M. H. Huang, *Small* **2019**, *15*, e1804726; b) J. Hu, H. He, L. Li, X. Zhou, Z. Li, Q. Shen, C. Wu, A. M. Asiri, Y. Zhou, Z. Zou, *Chem. Commun.* **2019**, *55*, 4777.
[12] P. Swetha, S. P. Feng, *Electrochem. Commun.* **2018**, *94*, 64.
[13] a) P. Liu, Y. Liu, S. Zhang, J. Li, C. Wang, C. Zhao, P. Nie, Y. Dong, X. Zhang, S. Zhao, G. Wei, *Adv. Opt. Mater.* **2020**, *8*, 2001072; b) S. K. Shil, F. Wang, K. O. Egbo, Z. Lai, Y. Wang, Y. Wang, D. Zhao, S. W. Tsang, J. C. Ho, K. M. Yu, *ACS Appl. Mater. Interfaces* **2021**, *13*, 35930.
[14] K. Prassides, P. Day, A. K. Cheetham, *Inorg. Chem.* **1985**, *24*, 545.
[15] Y. P. Lin, B. Xia, S. Hu, Y. Zhong, Y. E. Huang, Z. Z. Zhang, N. Wu, Y. W. Wu, X. H. Wu, X. Y. Huang, Z. Xiao, K. Z. Du, *Energy & Environmental Materials* **2020**, *3*, 535.
[16] U. K. N. Din, M. A. Mohamed, M. M. Salleh, T. H. T. Aziz, *J. Mater. Sci.: Mater. Electron.* **2022**, *33*, 13625.
[17] M. Mala, T. Appadurai, A. K. Chandiran, *Dalton Trans.* **2022**, *51*, 2789.
[18] A. Singh, S. Satapathi, *ACS Applied Electronic Materials* **2022**, *4*, 3440.
[19] G. Gouadec, P. Colomban, *Prog. Cryst. Growth Charact. Mater.* **2007**, *53*, 1.
[20] S. Bernardini, F. Bellatreccia, G. D. Ventura, A. Sodo, *Geostandard Geoanalytic Res* **2021**, *45*, 223.
[21] H. W. Clark, B. I. Swanson, *J. Am. Chem. Soc.* **1981**, *103*, 2928.
[22] N. Arulmozhi, *Doctoral Thesis*, Queen's University, Kingston **2018**.
[23] Y. Guo, C. Feng, S. Wang, Y. Xie, C. Guo, Z. Liu, N. Akram, Y. Zhang, Y. Zhao, J. Wang, *J. Mater. Chem. A* **2020**, *8*, 24477.